Nonlinear interaction between rain- and wind-induced air-water gas exchange

E. L. Harrison,[1] F. Veron,[2] D. T. Ho,[3] M. C. Reid,[4] P. Orton,[5] and W. R. McGillis[6,7]

Received 17 October 2011; revised 20 January 2012; accepted 27 January 2012; published 21 March 2012.

[1] The combined effects of rain and wind on air-water gas exchange were investigated with a series of experiments conducted at University of Delaware's Air-Sea Interaction Laboratory (ASIL). During this study, the third ASIL Wind and Rain Experiment (WRX 3), a combination of three rain rates and eight wind speeds were executed using aqueous mass balances of SF_6 to determine gas transfer velocities, $k(600)$. In addition, measurements of wave properties, currents, and turbulence were obtained. Study results show that rain and wind effects combine nonlinearly to enhance air-water gas exchange. Also, rainfall appears to contribute significantly to the total air-water gas flux at low wind speeds, while at higher speeds rain effects appear to be negligible. We find that the range of conditions over which the rain effects are important is well defined by the ratio of rain kinetic energy flux to that of the wind. A nonlinear parameterization of $k(600)$ for the combined effects of rain and wind is proposed. We extend this parameterization to field conditions and obtain the approximate rain rate and wind speed conditions where rain is expected to have a significant effect on air-sea gas exchange. Low wind speed–high rain rate regions such as the tropics are regions where rain is expected to play a significant role.

Citation: Harrison, E. L., F. Veron, D. T. Ho, M. C. Reid, P. Orton, and W. R. McGillis (2012), Nonlinear interaction between rain- and wind-induced air-water gas exchange, *J. Geophys. Res.*, *117*, C03034, doi:10.1029/2011JC007693.

1. Introduction

[2] Air-water gas exchange is an important process at local, regional, and global scales as it determines evasion of volatile pollutants, aqueous dissolved oxygen content, and cycling of biogeochemically important trace gases.

[3] Gas exchange for slightly soluble gases is limited by waterside resistance, and is therefore controlled by near surface turbulence [*Jähne et al.*, 1987] that is produced by environmental processes such as wind, waves and other events affecting subsurface mixing. Many parameterizations of wind speed and gas transfer velocity have been developed from both laboratory and field experiments [*Wanninkhof*, 1992; *Nightingale et al.*, 2000; *Ho et al.*, 2006]. However, these parameterizations typically do not distinguish between the individual turbulence generation mechanisms. In principle, it is possible to separate wind generated shear turbulence and that generated by other phenomena.

[4] The effects of rainfall on the near surface turbulence and the consequent air-sea gas exchange have typically been excluded from global air-sea flux parameterizations. The potential importance of rainfall to air-sea fluxes is illustrated by a simple estimate of the rain-induced stress based on rain rate and rain impact velocity [*Caldwell and Elliott*, 1971]. Under low wind speed and high rain rate conditions, typically found in the tropics, the momentum flux due to rain might be comparable to that provided by wind alone. Furthermore, assuming that the kinetic energy provided by rainfall dissipates in a shallow near surface layer [*Green and Houk*, 1979], we estimate that rain-induced dissipation compares in order of magnitude with that typically found under active breaking waves, indicating that rainfall can generate significant near surface turbulence (see Appendix A for details).

[5] Several studies investigated the relationships between several rainfall properties and gas exchange [*Ho et al.*, 1997, 2000, 2004, 2007; *Takagaki and Komori*, 2007; *Zappa et al.*, 2009], but only a few focused on the turbulence generated by rain [*Green and Houk*, 1979; *Tsimplis and Thorpe*, 1989; *Zappa et al.*, 2009]. Rain-induced gas exchange parameterizations in the absence of wind have been proposed as a function of both the kinetic energy flux of rain [*Ho et al.*, 1997, 2000] and the momentum flux [*Takagaki*

[1]Air-Sea Interaction Laboratory, School of Marine Science and Policy, College of Earth, Ocean, and Environment, University of Delaware, Lewes, Delaware, USA.
[2]College of Earth, Ocean and Environment, University of Delaware, Newark, Delaware, USA.
[3]School of Ocean and Earth Science and Technology, Department of Oceanography, University of Hawai'i at Manoa, Honolulu, Hawaii, USA.
[4]Department of Civil and Environmental Engineering, Princeton University, Princeton, New Jersey, USA.
[5]Stevens Institute of Technology, Hoboken, New Jersey, USA.
[6]Department of Earth and Environmental Engineering, Columbia University, New York, New York, USA.
[7]Also at Lamont-Doherty Earth Observatory of Columbia University, Palisades, New York, USA.

0148-0227/12/2011JC007693

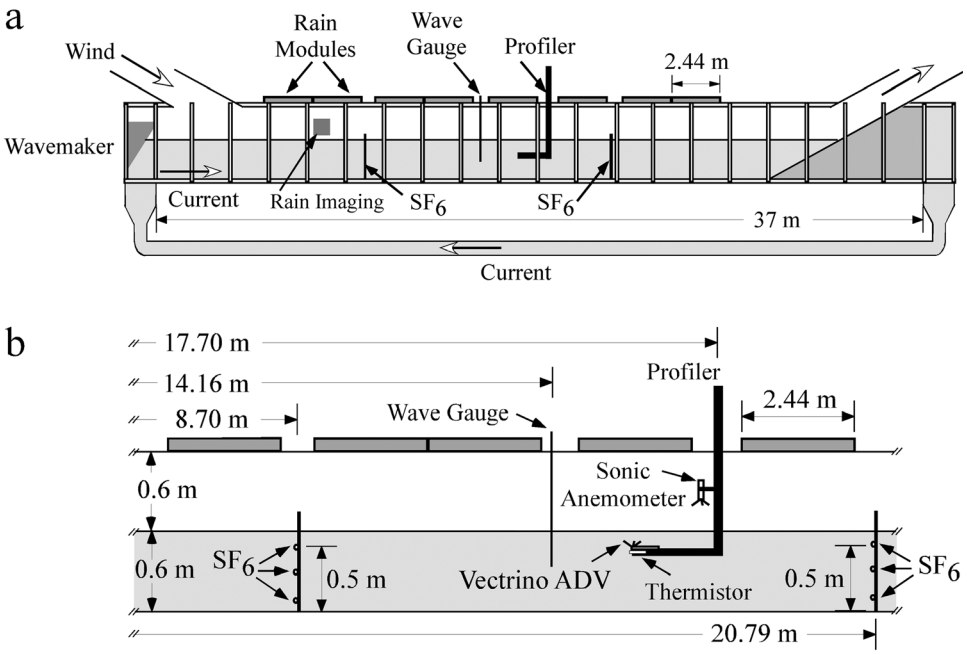

Figure 1. Schematics of (a) the wind-wave-current current flume at the Air-Sea Interaction Laboratory (ASIL) facility and (b) the instrumentation setup during WRX 3.

and Komori, 2007] for a wide-range of rainfall conditions. A series of saltwater experiments [*Ho et al.*, 2004] demonstrated that gas transfer velocities for rain on both freshwater and saltwater were comparable, with a reduction in the overall flux for the saltwater case due to stratification. The interaction and combined influence of rain and wind on air-water gas exchange were examined by *Ho et al.* [2007], but the experiment had some limitations such as rainfall only impacted approximately 3% of the flume's total surface area. *Turk et al.* [2010] incorporated the linear additive model of *Ho et al.* [2007] in a case study in the western equatorial Pacific Ocean to estimate the impact of rain on the CO_2 exchange and found that the inclusion of rain effects changed the area from a CO_2 source to a CO_2 sink.

[6] We address some of those limitations here with the results of the Wind and Rain Experiment 3 (WRX 3) conducted at the University of Delaware's Air-Sea Interaction Laboratory. These experiments were designed to systematically study the combined effects of rain and wind on air-sea gas exchange and included bulk gas transfer velocity measurements using waterside mass balances of sulfur hexafluoride, SF_6, along with measurements of wave properties, wind speed, and waterside turbulence.

2. Experiments

2.1. Setup

[7] The experiments were conducted in a wind-wave-current flume at the Air-Sea Interaction Laboratory (ASIL) of the University of Delaware. The flume is 1-m wide, 1.25-m high and 42-m long, with a 37-m long working section. The tank is equipped with a recirculating wind tunnel that is capable of generating wind speeds up to 17 m s^{-1} (approximately 24 m s^{-1} when scaled to a 10-m height). Currents up to 0.5 m s^{-1} can be generated using a recirculating pump. Both wind and currents are computer-controlled, which allows for stability and repeatability. The water temperature during the experiment campaign averaged 21.8 ± 0.7 °C. An artificial beach is permanently installed at the end of the flume to dissipate wave energy and eliminate wave reflections (Figure 1a). For these experiments, individual runs with nominal 10-m wind speeds, U_{10}, of 0, 3.5, 5.3, 8.6, 11.0, 14.1, 15.6 and 17.7 m s^{-1} were performed. A steady current of 5.3 cm s^{-1} was established in the flume using the recirculating pump to provide homogenization for the waterside concentration of SF_6. The current was experimentally verified to be uniform to a depth of 25 cm and the thickness of the boundary layer at the bottom of the flume is estimated to be on the order of O(5) mm.

[8] Rainfall was generated with 8 rain simulators that together covered 19.5 m of the flume's length (Figure 1). Approximately 20,000 hypodermic needles (Fine-Ject, 20 gauge) were randomly distributed among the rain simulators with ≈2500 needles per simulator. A water depth of 0.6 m provided a 0.6-m droplet fall height. Rain rates were changed by varying the constant head height within the rain simulators, leading to nominal rain rates, R, of 0, 30 and 60 mm h^{-1} (nominal rain rates are the rain rates produced by the rain simulators and then normalized by the total free surface area in the flume). Groundwater was stored in two large reservoirs within the laboratory, and was used to supply the rain simulators. The water used for rain was stripped of excess trace gases commonly found in groundwater (e.g., CO_2, CH_4, N_2O) by bubbling atmospheric air through the water using pond aeration systems (Sweetwater, KPA1-2), and was allowed to reach thermal equilibrium with the ambient conditions inside the laboratory. From the reservoirs, water was pumped to the rain simulators in which an overflow system maintained a constant head in the

Table 1. Experimental Conditions for the Two WRX 3 Campaigns[a]

Run	$U_{0.15}$ (m s^{-1})	U_{10} (m s^{-1})	u_* (m s^{-1})	R (mm h^{-1})	k(600) (cm h^{-1})	Run	$U_{0.15}$ (m s^{-1})	U_{10} (m s^{-1})	u_* (m s^{-1})	R (mm h^{-1})
G-10	0	0	0	0	0.8 ± 0.2	D-09	0	0	0	0
G-14	0	0	0	31.2	9.1 ± 0.4	D-26	0	0	0	25.8
G-08	0	0	0	60.8	12.2 ± 0.4	D-19	0	0	0	61.9
G-05	2.0	2.9	0.08	0	2.2 ± 0.2	D-08	2.1	3.4	0.12	0
G-03	1.9	3.2	0.13	21.4	7.8 ± 0.4	D-25	2.3	3.5	0.12	26.3
G-02	1.8	3.0	0.12	54.6	12.3 ± 0.3	D-20	2.2	3.7	0.14	59.0
G-06	3.3	5.1	0.18	0	5.1 ± 0.4	D-07	3.3	5.3	0.20	0
G-09	3.3	5.7	0.24	26.9	9.2 ± 0.3	D-24	3.5	5.2	0.17	27.1
G-18	3.3	5.9	0.25	59.7	13.5 ± 0.3	D-21	3.5	5.5	0.20	57.1
G-19	5.3	7.8	0.24	0	11.5 ± 0.4	D-06	5.5	8.5	0.30	0
G-13	5.5	8.8	0.33	31.3	14.6 ± 0.4	D-23	5.5	8.5	0.30	27.6
G-22	5.5	9.0	0.34	58.3	19.0 ± 0.4	D-22	5.5	8.9	0.33	54.7
G-25	7.5	11.3	0.37	0	20.5 ± 0.5	D-05	7.7	11.2	0.35	0
G-23	7.4	11.9	0.43	31.1	24.9 ± 0.5	D-31	7.4	11.1	0.37	28.1
G-21	7.4	12.2	0.47	60.6	25.0 ± 0.4	D-30	7.4	10.8	0.37	52.7
G-20	9.6	13.4	0.40	0	27.9 ± 0.3	D-04	9.6	14.0	0.43	0
G-04	9.6	14.0	0.43	17.1	25.6 ± 1.4	D-32	9.4	13.8	0.42	26.3
G-07	9.6	15.0	0.53	60.5	33.5 ± 0.3	D-29	9.5	14.4	0.48	54.2
G-15	10.5	15.1	0.44	0	34.3 ± 0.5	D-03	10.4	15.7	0.51	0
G-24	10.5	16.1	0.55	25.8	36.1 ± 0.6	D-33	10.4	15.1	0.46	23.8
G-26	10.4	16.3	0.57	63.6	44.2 ± 0.4	D-28	10.4	16.0	0.54	58.7
G-12	11.3	17.8	0.64	0	40.8 ± 0.6	D-02	11.2	17.8	0.65	0
G-01	11.1	18.0	0.68	30.1	39.0 ± 0.4	D-34	11.3	17.8	0.64	22.4
G-11	11.3	18.8	0.73	57.9	46.9 ± 0.4	D-10	11.2	17.4	0.61	55.6

[a]*G* indicates a gas campaign experiment while *D* indicates a dynamics campaign experiment. $U_{0.15}$ and U_{10} are the wind speed values at heights of 0.15 m and 10 m above the water surface calculated using equation (1), respectively. The friction velocity, u_*, average rain rate, *R*, and the gas transfer velocity measured using a mass balance technique with SF_6, *k*(600), are detailed for each experiment. There were some small disparities between the U_{10} values for the gas exchange and dynamics experimental campaigns observed that are attributed to normal experimental variability.

simulator with the excess water returned to these reservoirs. The water level inside the flume was kept at a constant height by pumping the excess water (from the rain) to a separate storage reservoir. The pump was triggered manually and the flow rate was monitored with a digital flowmeter.

[9] Combining rain rates and wind speeds led to a total of 24 individual runs (including null cases). During each run, both the wind field and the rain were allowed to achieve steady state conditions (the wind field was fully developed in the flume, the rain rate was consistent in all rain simulators, and the wave field was fetch limited) prior to the first measurement. Taking advantage of the repeatability of the computer-controlled winds and currents, the study was divided into two sets of experiments. The first set focused on gas exchange measurements and is labeled "G", while the second focused on the remaining dynamics measurements, "D" (see Table 1). The separation into two campaigns allowed for underwater turbulence and velocity measurements to be further refined near the surface. For the gas exchange experiments, each run lasted approximately 3 h, and wind speed profiles, wave height, rain rate, raindrops' fall velocity and size, waterside velocity profiles, and both airside and waterside SF_6 concentrations were measured. During the dynamics experiments, each run lasted approximately 1 h, and wind speed profiles, wave height, rain rate, and waterside velocity profiles were measured. Waterside turbulence measurements were also made to examine the momentum transfer by rain and wind to the water.

2.2. Methods

2.2.1. Rain Properties

[10] The average rain rates were measured by quantifying the water overflow from the flume with a digital flowmeter (Proteus Industries, Inc., 0812BN19). The spatially averaged rain rate was calculated by dividing the volume of water removed by the elapsed rain time and by the surface area of the flume (39.24 m^2, see Figure 1a). Raindrop size and impact velocity were determined by examining images taken with a high speed digital camera (Phantom 5.1), located at a fetch of 22.45 m (Figure 1a). The camera provided an image size of 9.3 × 9.3 cm and a pixel resolution of 90.7 μm. The field of view was illuminated with a 30.5 × 20.3 cm continuous fluorescent backlight. Six four-second video records were acquired per run at a frame rate of 1000 Hz. Rain rate, drop radius, and horizontal and vertical impact velocity were measured for all rain experiments.

2.2.2. Wind, Waves, and Currents

[11] The wind speed in the flume was measured with a 2D sonic anemometer (Gill, Wind Observer II) and sampled at 1 Hz. The sonic anemometer was mounted on an A-frame profiler at a fetch of 17.6 m and offset by 19 cm from the centerline of the flume to avoid interference with other instruments mounted on the profiler. The wind profiles spanned heights from 3.5–27 cm above the still water level, and the upper part of the profiles, away from the influence of the waves, were found to follow the classical "law of the wall" log layer:

$$U_a(z) = \frac{u_*}{\kappa} \ln\left(\frac{z}{z_0}\right), \tag{1}$$

where U_a is the wind speed, u_* is the airside friction velocity, z is the height above the water surface, z_0 is the roughness length and κ is the von Kármán constant (≈0.4). A logarithmic regression was applied to the profiled wind speed data to obtain values for u_* and z_0.

[12] Waves in the flume were measured with a capacitance wave gauge and the signal was sampled at 200 Hz with a 16-bit A/D board (National Instruments, PCI-MIO-16XE-10). The wave gauge was located at a fetch of 14.2 m, 0.4 m downwind of the third rain simulator and 0.3 m upwind of the fourth rain simulator. The wave gauge was placed 0.28 m away from the centerline of the flume and calibrated prior to the first experiment of each day. No drift in the calibration was observed. Spectra of the wave height were calculated for 50-min records (600,000 points) using Hanning windows of 5.14 s (1024 points) with a 50% overlap. It was found that the wave field did not vary during the runs and 50-min records were therefore sufficiently representative of the wave conditions.

[13] Waterside velocity profiles were measured using a three-dimensional acoustic Doppler velocimeter (ADV, Nortek Vectrino). The ADV's side-looking cable probe was mounted on the long arm of the A-frame profiler, which extended beneath the fifth rain simulator, at a fetch of 16.2 m. The waterside velocity profiles spanned heights from 2.9–24.9 cm beneath the still water level, the signal was sampled at 200 Hz, and the instrument had a measurement volume of 0.2 cm^3. During the detailed dynamics campaign, measurements were taken at 10 water depths per experimental run, with 4.5-min time series recorded for each water depth. Mean velocity profiles were computed by taking the average of the 4.5-min record for each measurement height.

[14] A set of five thermistors (RBR TR-1050) were used to monitor air and water temperature and check for consistency among the 24 experiments. One was mounted on the long arm of the A-frame profiler, at a fetch of 16.8 m, to measure water temperature at multiple heights. A second was placed downwind, at a fetch of 28.1 m and a constant water depth of 0.25 m. Two others were used to measure air temperature 0.1 m above the still water level, at fetches of 8.7 and 20.8 m. A final one was located in one of the rainwater reservoirs to monitor rainwater temperature. All thermistors were sampled at 0.167 Hz, and temperatures were found to be consistent in the flume air, flume water and rainwater.

2.2.3. Turbulence

[15] Turbulence measurements were obtained from the fast underwater ADV. The sampling rate of 200 Hz allowed for the resolution of frequencies on both sides of the surface wave peak frequency. Here, the signal with the least noise was used for turbulence measurements; this was the velocity component that was oriented vertically upwards (the other two velocity components, streamwise and spanwise are slightly more noisy). This choice was supported by the observation of no significant differences between orientations in the frequency ranges of the velocity spectra used in the turbulence calculation detailed below.

[16] For isotropic turbulence with a sufficiently large Reynolds number, the wavenumber spectrum of the turbulence, $S(k_w)$, exhibits an inertial range that separates the energy containing scales from the scales at which energy is dissipated by viscous forces. In the inertial range, the energy is conserved and simply "cascades" down to smaller scales. Under these conditions the inertial range of the wavenumber spectrum has a form that is proportional to $S(k_w) \propto k_w^{-5/3} \varepsilon^{2/3}$. The turbulent kinetic energy dissipation rate, ε, can be directly estimated from the level of the measured spectrum. When the mean advecting flow also contains oscillatory motion from the waves, the Taylor frozen field hypothesis, which is generally used to transform a frequency spectrum into a wavenumber spectrum, needs to be modified [*Lumley and Terray*, 1983]. Here, the one-dimensional turbulent vertical velocity frequency spectra, $S_{ww}(f)$, were calculated for each 4.5-min record (54,000 points) using Hanning windows of 5.14 s (1024 points) with a 50% overlap. Then, we estimated ε at each height from

$$S_{ww}(f) = \frac{7}{110} 2^{4/3} \Gamma\left(\frac{1}{3}\right) \left(\frac{8\varepsilon}{9\alpha_H} \frac{U_{rms}^{orb}}{2\pi}\right)^{2/3} f^{-5/3}, \qquad (2)$$

where U_{rms}^{orb} is the orbital velocity used in the case of unsteady advection and α_H, Heisenberg's constant, is ≈0.4 [*Veron and Melville*, 1999]. We note here that while no significant difference in the turbulence, between velocity orientations were observed, we do not anticipate the assumption of isotropy to hold in the vicinity of the interface. We do however believe that this assumption is not significantly limiting below the wave where our measurements were made [*Gemmrich and Farmer*, 2004].

2.2.4. Gas Transfer Velocities

[17] Gas transfer velocities were determined with the waterside mass balance of SF_6 [*Ho et al.*, 1997]. Daily tracer injections were necessary during WRX 3 because of the high turnover rate of the flume's water. Tracer injections were performed each evening to allow the flume's water to be mixed overnight by the recirculating pump-driven current. Using a 60-ml plastic syringe, 180–950 nmol (nmol = nanomol = 10^{-9} mol) of SF_6 dissolved in water was injected into the flume.

[18] During the experiments, the SF_6 was sampled every 20 min at 3 different water depths (0.1, 0.3, and 0.5 m beneath the still water level), and at two locations in the flume (8.7 and 20.8 m fetch). The samples were taken with 50-ml glass syringes attached to a 3-way valve using 0.3175-cm ID flexible tubing. For each sample, the valve was opened and the water drawn slowly into the syringe. Extreme care was taken to prevent the occurrence of bubbles in the sampling line or in the syringe, and no samples were kept for analysis when bubbles were seen in either the tubing or the syringe. The samples were analyzed using a headspace method described in detail by *Wanninkhof et al.* [1987]. A predetermined amount of water (10 to 30 ml) was drawn into the syringe during sampling, and then a headspace (40 to 20 ml) was created with ultra-high purity (UHP; 99.999%) N_2. Next, after at least 3 minutes of vigorous shaking on a mechanical wrist action shaker to equilibrate the water with the N_2 in the headspace, the gas sample was pushed through a drying column of $Mg(ClO_4)_2$ into a sample loop. The SF_6 was then separated from other gases using molecular sieve 5A column at room temperature. Following this the gas sample was passed to a gas chromatograph (GC) equipped with an electron capture detector (ECD) using UHP N_2 as the carrier.

[19] Using the total rate of change in mean SF_6 concentration, C, in the flume, the gas flux across the air-water interface, F, is estimated using

$$F = h \frac{dC}{dt}, \qquad (3)$$

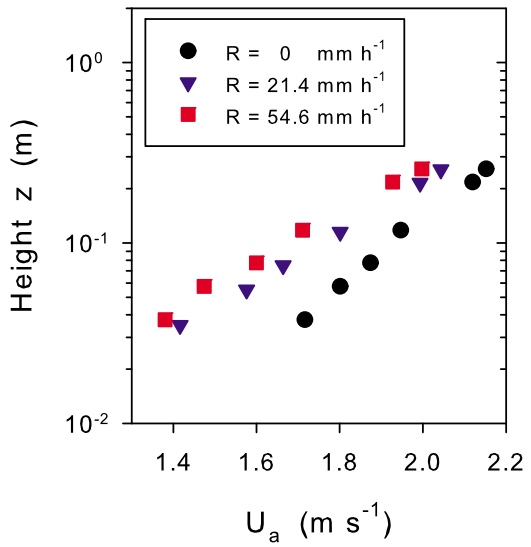

Figure 2. With an identical pressure gradient driving the wind field, the measured mean wind speed profiles, $U_a(z)$, are observed to change with rain rate.

where h is the mean water depth in the flume. The gas transfer velocity, k, is calculated from

$$k = \frac{F}{C_w - \alpha C_a}, \tag{4}$$

where C_w is the SF_6 concentration of the water directly beneath the air-water interface, C_a is the SF_6 concentration in the headspace of the flume, and αC_a is the solubility equilibrium for SF_6 in the water. If the water is well mixed with respect to tracer concentration, equations (3) and (4) can be combined, assuming $C_w = C$, and then integrated over the elapsed time, Δt, to obtain

$$k = \frac{h}{\Delta t} \ln\left(\frac{C_i - \alpha C_a}{C_f - \alpha C_a}\right), \tag{5}$$

where C_i and C_f are the initial and final mean tracer concentrations, respectively.

[20] The observed reduction in total tracer concentration in the water during each experiment, however, was due to both gas exchange at the air-water interface and dilution of tank water by nominally SF_6-free rain. In order to calculate k accurately, the effect of dilution must be eliminated. This can be achieved using a dilution model described in detail by *Ho et al.* [1997, 2000]:

$$k = \frac{h}{\Delta t} \ln\left(\frac{C_i - \alpha C_a}{C_f - \alpha C_a}\right) - \frac{hP}{V}, \tag{6}$$

where P is the rain volume rate and V is the volume of water in the flume.

[21] The gas transfer velocities calculated for SF_6 were normalized to a Schmidt number, the ratio of kinematic viscosity of the water to diffusivity of the gas in water, Sc, of 600, corresponding to the value for CO_2 in freshwater at 20°C:

$$k(600) = k_{SF_6}\left(\frac{600}{Sc(SF_6)}\right)^n. \tag{7}$$

Here k_{SF_6} and $Sc(SF_6)$ are the gas transfer velocity and the Schmidt number for SF_6, respectively. $Sc(SF_6)$ was 886 during the present experiment. It has been shown in models and experiments, that for a clean wavy water surface, in the absence of bubbles, n equals $-1/2$ [*Brumley and Jirka*, 1987; *Jähne et al.*, 1984; *Ledwell*, 1984].

3. Results

3.1. Wind, Waves, Currents, and Turbulence

[22] As described above, we used wind speed measurements from the sonic anemometer and the law of the wall (equation (1)) to estimate u_* and the equivalent 10-m height wind speed U_{10}. Buoyancy effects were also incorporated into the u_* computations using Monin-Obukhov similarity theory (MOST). In all cases, the conditions were nearly neutral and the measured u_* was always within 3% of the corresponding neutral estimate.

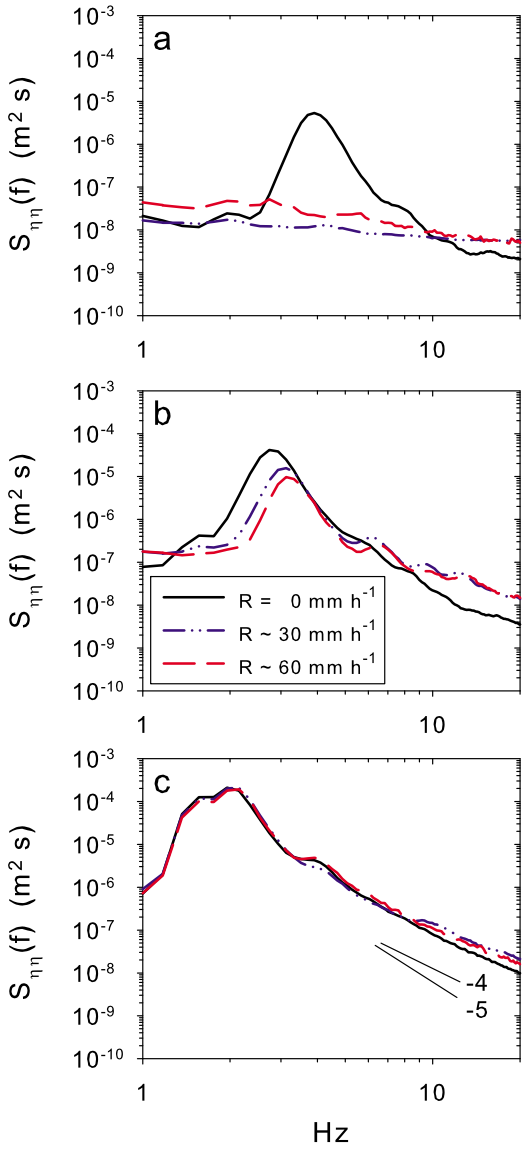

Figure 3. Measured wave height frequency spectra, $S_{\eta\eta}(f)$, for all R and U_{10} of (a) 5.3 m s^{-1}, (b) 8.6 m s^{-1}, and (c) 14.1 m s^{-1}.

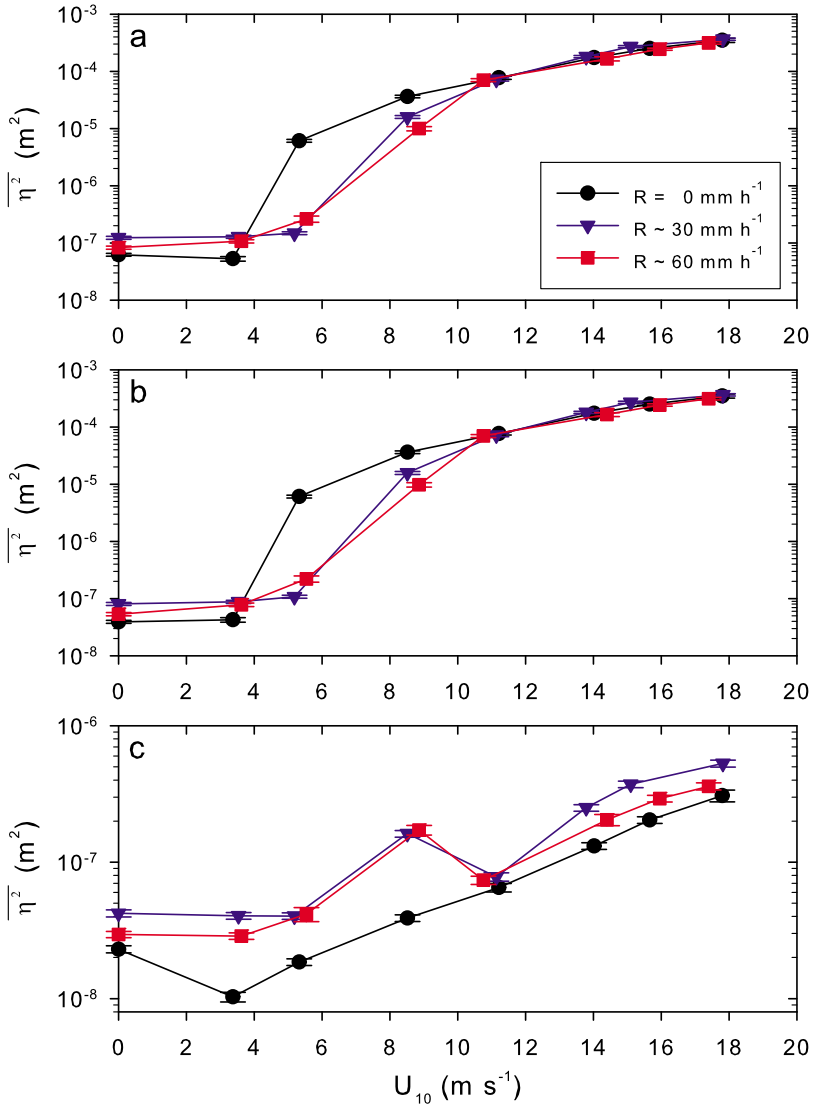

Figure 4. The wave height variance, $\overline{\eta^2}$, as a function of U_{10} for all R, calculated for the frequency ranges of (a) $1 < f < 20$ Hz, (b) $1 < f < 13.4$ Hz, and (c) $13.4 < f < 20$ Hz. Error bars were estimated using equation (8) and the 95% confidence interval wave height frequency spectra.

[23] We observed an increase in u_* with increasing rain rate R for each wind speed (Table 1). This is illustrated in Figure 2, which shows the mean wind speed profiles measured at the lowest nonzero wind condition for various rain rates. At equivalent wind fan rotation rates, the mean wind speed decreased in the presence of rain indicating that a significant amount of momentum was taken from the total available (and constant) energy in the wind field and imparted to the raindrops. The drops started with zero horizontal velocity at the top of the flume's airspace, and were accelerated by the wind field as they fell. This loss of energy by the wind, which increased with R (more mass loading from the rain), resulted in the observed increase in u_*. It should be noted, however, that this behavior is in contrast to what occurs in the field, where raindrops enter the boundary layer with their maximum horizontal velocity and then decelerate thereby adding energy to the wind.

[24] Wave height frequency spectra, $S_{\eta\eta}(f)$, for U_{10} of 5.3, 8.6 and 14.1 m s^{-1} are shown in Figure 3. At a low wind speed of 5.3 m s^{-1}, the observed wave peak, 4 Hz, was completely damped at both nonzero rain rates; with increasing rain rates there is also a significant increase in energy at high frequency. For a moderate wind speed of 8.6 m s^{-1}, the observed wave peak was only partially damped, with the amount of damping increasing with an increasing R. There is no significant wave damping observed at U_{10} greater than approximately 11 m s^{-1}, but there was still an increase in high frequency wave energy observed under rain conditions. These results are consistent with previous rain-induced wave damping experiments [*Tsimplis and Thorpe*, 1989; *Poon et al.*, 1992; *Tsimplis*, 1992; *Yang et al.*, 1997; *Braun et al.*, 2002; *Ho et al.*, 2007] where it was observed that the gravity range of the spectrum is damped by rainfall while additional capillary waves (high frequency) are generated by the raindrop impacts on the surface in the form of ring waves. Regardless of rain conditions, the wave peak also shifted towards lower frequencies with increasing wind speed as

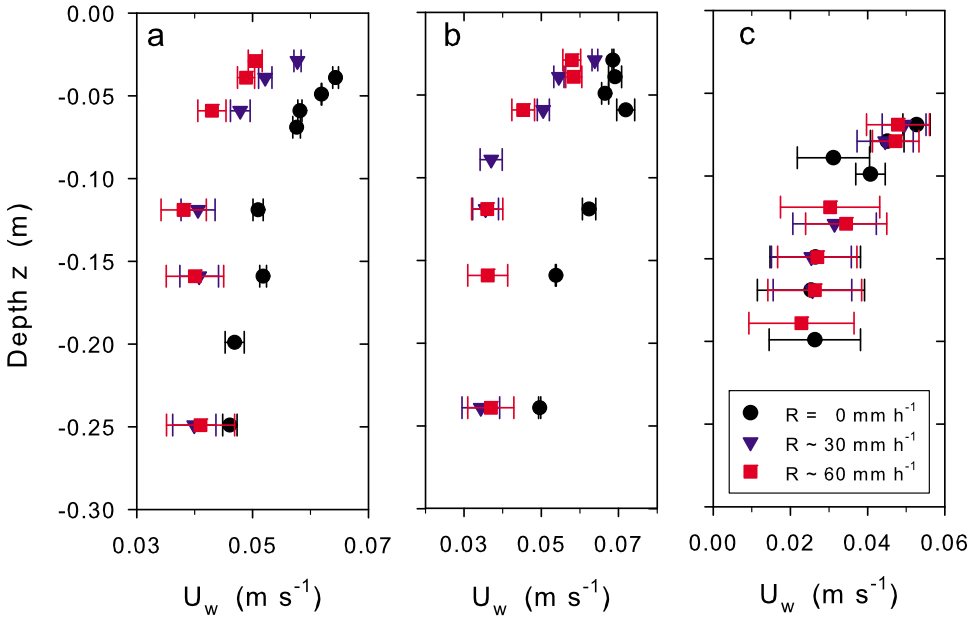

Figure 5. Waterside mean horizontal velocity profiles, $U_w(z)$, as a function of R for U_{10} of (a) 3.5 m s^{-1}, (b) 5.3 m s^{-1}, and (c) 14.1 m s^{-1}.

expected, with the high frequency tail of the spectrum falling off with a -5 to -4 slope.

[25] Another way to examine the wave height data is to calculate the wave height variance, $\overline{\eta^2}$, for different frequency bands:

$$\overline{\eta^2} = \int_{f_1}^{f_2} S_{\eta\eta}(f)df, \tag{8}$$

where f_1 and f_2 are the lower and upper frequency limits of integration, respectively. The wave height variance has been computed here for frequency ranges of $1 < f < 20$ Hz, $1 < f <$ 13.4 Hz, and $13.4 < f < 20$ Hz (Figure 4). The cutoff frequency of 13.4 Hz marks the transition between capillary and gravity ranges. While rain generated ring waves have peak frequencies between 4 to 6 Hz [*Bliven et al.*, 1997], they also generate a significant amount of energy at even higher frequencies. The frequency range of $13.4 < f < 20$ Hz illustrates this high frequency rain-generation. For the full frequency range, $1 < f < 20$ Hz, there was an initial increase in $\overline{\eta^2}$ at very low wind speeds where rain-generated surface ring waves dominated the wave height spectrum. This was followed by a significant decrease in $\overline{\eta^2}$ for wind speeds up to approximately 11 m s^{-1}; at higher wind speeds there is no significant effect of rain on $\overline{\eta^2}$. Reducing the frequency range to $1 < f <$ 13.4 Hz suggests that damping of the primary wave peak by rain was the dominant effect in reducing the overall surface height variance. In addition, while there did not appear to be a difference in the results between the total and low frequency values of $\overline{\eta^2}$, for $13.4 < f < 20$ Hz, the high frequency range of the wave height spectrum was systematically enhanced by the rain for all wind speeds and rain rates examined here.

[26] Waterside mean horizontal velocity profiles, $U_w(z)$, were calculated for all experiments and the profiles for U_{10} of 3.5, 5.3 and 14.1 m s^{-1} are shown in Figure 5. At low to moderate wind speeds, U_w decreased significantly throughout the water column with increasing R. We find this result initially counterintuitive as we expect the additional horizontal momentum flux from the rain to participate in the generation of near surface currents. The reduction in surface currents is likely to be a consequence of two effects. The first is the reduced wave activity and the resultant reduction in Stokes drift. However, estimates of the Stokes drift from the wave height spectra (Figure 3) indicate this effect is significantly smaller than the decreases observed in U_w. The second consequence, first described by *Reynolds* [1875], is that as the raindrops penetrate the water column they disrupt the current and/or wave field and act as physical barrier to that flow due to their limited horizontal momentum in comparison to the background flow field. The energy lost to overcoming the resistance from penetrating raindrops results in the observed decreases in U_w.

[27] Vertical velocity frequency spectra ($S_{ww}(f)$, Figure 6) show a similar behavior to the wave height frequency spectra. At a low wind speed of 5.3 m s^{-1} and a measurement depth of -3.9 cm, the strong wave-associated peak was dampened by rain. There was also an increase in the energy within the inertial subrange, with an approximate $-5/3$ slope, observed under rain conditions. At a slightly higher U_{10} of 8.6 m s^{-1} and a measurement depth of -3.9 cm, the wave-associated peak in $S_{ww}(f)$ was only partially dampened with the amount of damping increasing with increasing R. An increase in the energy within the inertial subrange was also observed; again, higher turbulence levels within that frequency range are observed with higher rain rates. At wind speeds higher than approximately 11 m s^{-1}, there was no significant effect of rain near the wave-associated peak and minimal differences in energy seen in the inertial subrange.

[28] Applying equation (2) to the vertical velocity frequency spectrums at all measurement depths yielded profiles of turbulent kinetic energy dissipation, $\varepsilon(z)$. The background flume current was removed from U_{RMS}^{orb} by subtracting U_w.

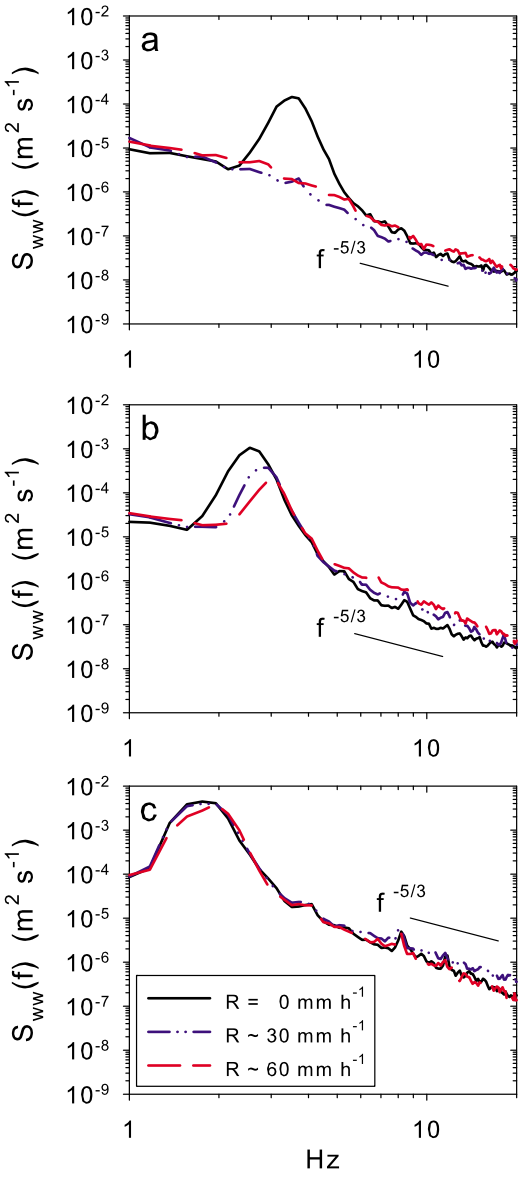

Figure 6. Vertical velocity frequency spectra, $S_{ww}(f)$, for all R, and U_{10} and z of (a) U_{10} = 5.3 m s^{-1} and z = −3.9 cm, (b) U_{10} = 8.6 m s^{-1} and z = −3.9 cm, and (c) U_{10} = 14.1 m s^{-1} and z = −6.9 cm.

The measured $\varepsilon(z)$ profiles for U_{10} of 0, 3.5, and 14.1 m s^{-1} are shown in Figure 7. For no wind conditions, ε increased throughout the water column with increasing R. At a low wind speed of 3.5 m s^{-1}, ε was higher under rain conditions near the surface but did not vary significantly at depth. For wind speeds greater than approximately 11 m s^{-1}, there was no significant effect of rain on ε. It should be noted that the ADV's relatively large measurement volume for a turbulence measurement, 0.2 cm^3, limits the resolution of the small-scale turbulence that can be resolved here. However, ε is calculated from the inertial range which does not depend on the resolving the dissipation scale.

[29] All of the dynamics cases presented here (wave, currents and turbulence) exhibited an approximate 11 m s^{-1} cutoff wind speed for rain effects.

3.2. Gas Transfer Velocities

[30] Gas transfer velocities, determined from the SF_6 evasion technique, normalized to a Sc of 600, $k(600)$, are presented in Figure 8. In the cases where rain is not present, $k(600)$ increases with wind speed on a quadratic manner consistent with previous gas transfer measurements in flumes or in the field [*Wanninkhof*, 1992; *Nightingale et al.*, 2000; *Ho et al.*, 2006]. When rain is present, there is a strong increase in $k(600)$ observed with increasing R at low wind speeds. For example, with no wind and $R \approx 60$ mm h^{-1}, $k(600)$ was 12.2 cm h^{-1}. Expressed differently, with a rain rate of $R \approx 60$ mm h^{-1}, $k(600)$ was systematically an order of magnitude higher than experiments with no rain and wind speeds lower than ≈5.5 m s^{-1}. As the wind speed increases, the effects of the rainfall on $k(600)$ diminishes and at wind speeds higher than approximately 11 m s^{-1}, there was no significant effect of the rain on $k(600)$. The two outliers at high wind speeds, as indicated by their symbol sizes, had rain rates that varied significantly from the typical 30 or 60 mm h^{-1} values. These results differ somewhat from those of *Ho et al.* [2007], who showed that the effects of rain and wind were linearly additive over the whole range of wind and rain conditions they studied, which overlaps with the ones presented here. This will be discussed further below.

4. Discussion

4.1. Scaling $k(600)$ With the Kinetic Energy Flux of Rain

[31] Because rain-induced gas transfer is primarily due to rain-generated turbulence [*Ho et al.*, 2000], the gas transfer velocity from rain, $k(600)_r$, is well parameterized by the energy input from rain, characterized either as the momentum flux [*Takagaki and Komori*, 2007] or the kinetic energy flux of rain [*Ho et al.*, 1997, 2000, 2007], regardless of drop size and impact velocity. We choose here to look at the kinetic energy flux for reasons that will become apparent in the following section. For the case of a monodisperse drop size distribution, the vertical kinetic energy flux from rain, KEF_r, is easily estimated:

$$KEF_r = \frac{1}{2}\rho_d w^2 R, \tag{9}$$

where ρ_d is the density of the raindrops and w is their vertical impact velocity. The average values for drop radius, r, vertical impact velocity and percent terminal velocity, $\%w_t$, were 1.45 mm, 3.13 m s^{-1} and 39.3%, respectively. A summary of all rain parameters, including KEF_r, is found in Table 2. For a given R, KEF_r is approximately constant with wind speed.

[32] Figure 9 shows $k(600)$ as a function of KEF_r for experiments with no wind. The results from WRX 3 are consistent with results from previous rain-induced gas exchange experiments [*Ho et al.*, 1997, 2000, 2007]. These combined data suggest, when fitted with a two parameter power law, that

$$k(600)_r = 63.02(KEF_r)^{0.6242}, \tag{10}$$

where KEF_r and $k(600)r$ have the units of J m^{-2} s^{-1} and cm h^{-1}, respectively. This power law fit has an r^2 of

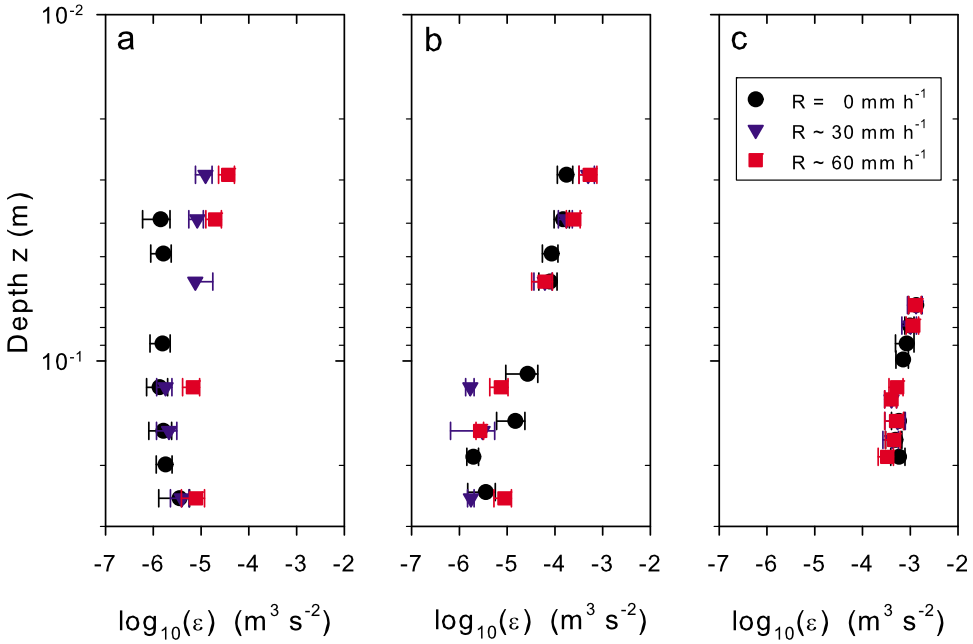

Figure 7. Turbulent kinetic energy dissipation profiles, $\varepsilon(z)$, for all R and U_{10} of (a) 0 m s^{-1}, (b) 3.5 m s^{-1}, and (c) 14.1 m s^{-1}.

0.9749, which is similar to the r^2 of a quadratic fit (0.9733).

[33] We next compare $k(600)$ with those estimated from equation (10). Figure 10 shows that estimated values of $k(600)_r$ (the gas transfer velocity due to rain alone) represent a large fraction of the total $k(600)$ at low wind speeds. This suggests rain effects dominate the gas transfer processes at these wind speeds. At wind speeds higher than approximately 11 m s^{-1} the rain contribution to the total $k(600)$ becomes a small, but still non-negligible, fraction of the total transfer velocity. The fact that at high wind speeds, rain and wind combine in a nonlinear way to influence gas exchange appears to depart from the results of *Ho et al.* [2007], but we will show below that this is in fact not the case.

[34] Heretofore the KEF_r scaling argument has only been applied to gas exchange results. The effect of the limited droplet fall height and consequential lower than terminal impact velocities has not been discussed in terms of the

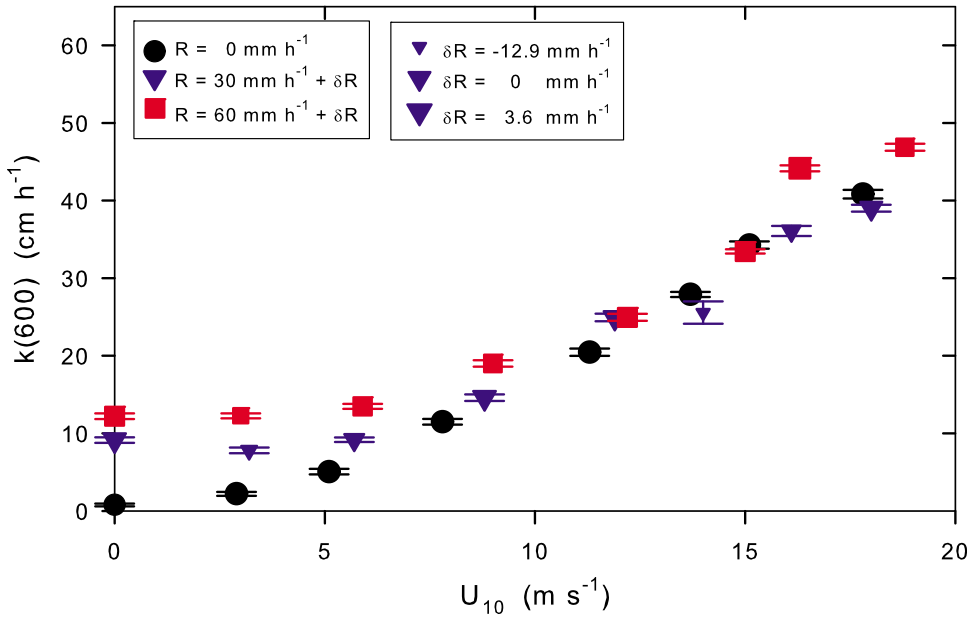

Figure 8. The gas transfer velocity, $k(600)$, calculated using the SF_6 evasion technique as a function of U_{10}. Symbol size indicates each experiment's rain rate variation, δR, from either 30 or 60 mm h^{-1} with smaller and larger symbols reflecting below and above average rain rates, respectively.

Table 2. Rain Properties for All Nonzero Rain Experiments During the WRX 3 Gas Campaign[a]

Run	U_{10} (m s^{-1})	R (mm h^{-1})	r (mm)	u (m s^{-1})	w (m s^{-1})	$\%w_T$ (%)	KEF_r (J m^{-2} s^{-1})
G-14	0	31.2	1.45	0	3.36	42.1	0.0488
G-08	0	60.8	1.46	0	3.32	41.8	0.0928
G-03	3.2	21.4	1.44	0.26	3.37	42.3	0.0337
G-02	3.0	54.6	1.45	0.25	3.29	41.3	0.0818
G-09	5.7	26.9	1.44	0.53	3.33	41.9	0.0413
G-18	5.9	59.7	1.46	0.54	3.30	41.3	0.0900
G-13	8.8	31.3	1.42	1.12	3.19	40.3	0.0441
G-22	9.0	58.3	1.44	1.16	3.17	39.8	0.0811
G-23	11.9	31.1	1.43	1.87	2.75	34.7	0.0326
G-21	12.2	60.6	1.46	1.84	3.08	38.5	0.0796
G-04	14.0	17.1	1.42	3.07	2.99	37.8	0.0211
G-07	15.0	60.5	1.45	2.88	3.01	37.8	0.0759
G-24	16.1	25.8	1.46	3.74	3.05	38.4	0.0333
G-26	16.3	63.6	1.47	3.56	3.01	37.6	0.0798
G-01	18.0	30.1	1.46	4.43	2.91	36.4	0.0353
G-11	18.8	57.9	1.44	4.65	2.93	36.8	0.0688

[a]The 10 m wind speed, U_{10}, rain rate, R, raindrop radius, r, the vertical and horizontal components of the raindrop impact velocity, u and w, percent terminal velocity, $\%w_r$, and the kinetic energy flux of rain, KEF_r, are listed for each experiment.

dynamics. First, the mechanics of the drop impacts can be shown to be similar at both our reduced impact velocity and at terminal velocity using the We-Fr diagram assembled by *Liow* [2001, Figure 17] by calculating the Weber number, We, and Froude number, Fr. The mean drop size and mean impact velocity yield values of 389 and 344 for We and Fr, respectively (see Appendix A for calculation details). The We and Fr values for the same drop size falling at terminal velocity are $O(10^3)$. In both cases, however, *Liow* [2001] indicates that upon impact, the drops will form a jet as the cavity generated by impact collapses, with spray generation and secondary bubble entrainment occurring. Second, if we assume from the similar wind speed cutoff observed in both the gas exchange and dynamics results, that KEF_r can potentially be used to scale the dynamics results as well, we may estimate what differences may be observed if the drops were impacting at terminal velocity. A velocity scale for the turbulence generated by rain, u_r, can be estimated by $KEF_r = \rho_w u_r^3$, where ρ_w is the density of the flume water. An evaluation of this parameterization indicates that drops impacting at terminal velocity should result in higher values of turbulent kinetic energy in the water column being produced compared to our lower impact velocities which likely would enhance the rain effects seen in both the current and waves data presented here. The exact relationship however between impact velocity and turbulence level will be addressed in subsequent experiments.

4.2. Thresholding Rain Effects and a Nonlinear Model for $k(600)$

[35] While the $k(600)$ results (Figure 8) do not appear to corroborate the linearly additive results for wind and rain effects seen by *Ho et al.* [2007], an investigation of which parameter controls the limit for rain effects yields an interesting result.

[36] Both the gas exchange and dynamics data (waves, currents and turbulence) presented here exhibited a consistent cutoff wind speed for rain effects of approximately 11 m s^{-1}. Gas exchange rates have been shown to be well correlated with wind stress and the friction velocity, u_* [*Wanninkhof et al.*, 2009]. In the previous section, we demonstrated that rain-induced gas exchange rates scale well with KEF_r. Therefore, to better understand this observed regime change at approximately 11 m s^{-1}, we compared KEF_r to the wind-imparted kinetic energy flux, $KEF_w = \rho_a u_*^3$, using the parameter β:

$$\beta \equiv \frac{KEF_r}{KEF_w}. \tag{11}$$

Figure 11 shows β for the data analyzed here, along with the data from the WRX 1 experiment of *Ho et al.* [2007]. For wind speeds less than 11 m s^{-1} in the present study, β is greater than one, and at wind speeds greater than 11 m s^{-1}, β is always less than one; i.e. this then suggests that rain influences the gas transfer (and the dynamics of the waves and near surface turbulence) in a significant manner if $\beta > 1$.

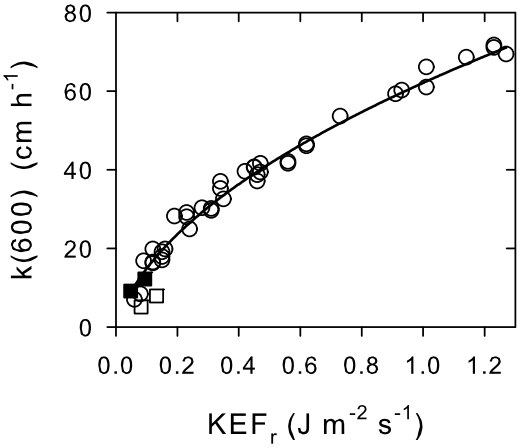

Figure 9. Rain induced gas transfer velocity measurements completed using the SF_6 evasion method during no wind, rain experiments as a function of the vertical kinetic energy flux of rain, KEF_r. The results from experiments completed at NASA's RainSea Interaction Facility are shown with open circle symbols [*Ho et al.*, 1997, 2000]. The results from two experimental campaigns completed at ASIL are shown with open and solid square symbols for WRX 1 from *Ho et al.* [2007] and WRX 3 (the present study), respectively.

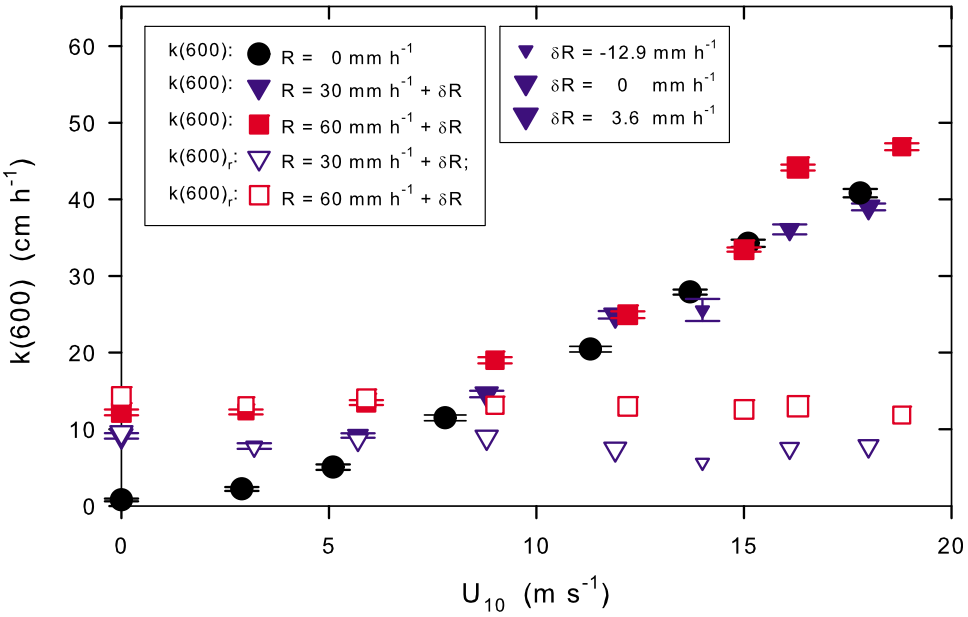

Figure 10. A comparison of the rain-induced gas transfer velocities, $k(600)_r$, estimated using equation (10) to the measured values calculated using the SF_6 evasion technique, $k(600)$, as a function of U_{10}. Symbol size indicates each experiment's rain rate variation, δR, from either 30 or 60 mm h^{-1} with smaller and larger symbols reflecting below and above average rain rates, respectively.

[37] Employing β as a predictor for rain effects on gas exchange suggests that the results from WRX 3 are, in fact, not inconsistent with those of *Ho et al.* [2007]. While the experiments conducted by *Ho et al.* [2007] had similar wind speeds and similar or lower nominal rain rates than WRX 3, the rain simulator was 2 m higher than the present study and the raindrops would have had higher vertical impact velocities. Consequently for the same rain rate as WRX 3, WRX 1 would have had a higher KEF_r. So, for the WRX 1 data set, experiments of *Ho et al.* [2007], with the exception of one

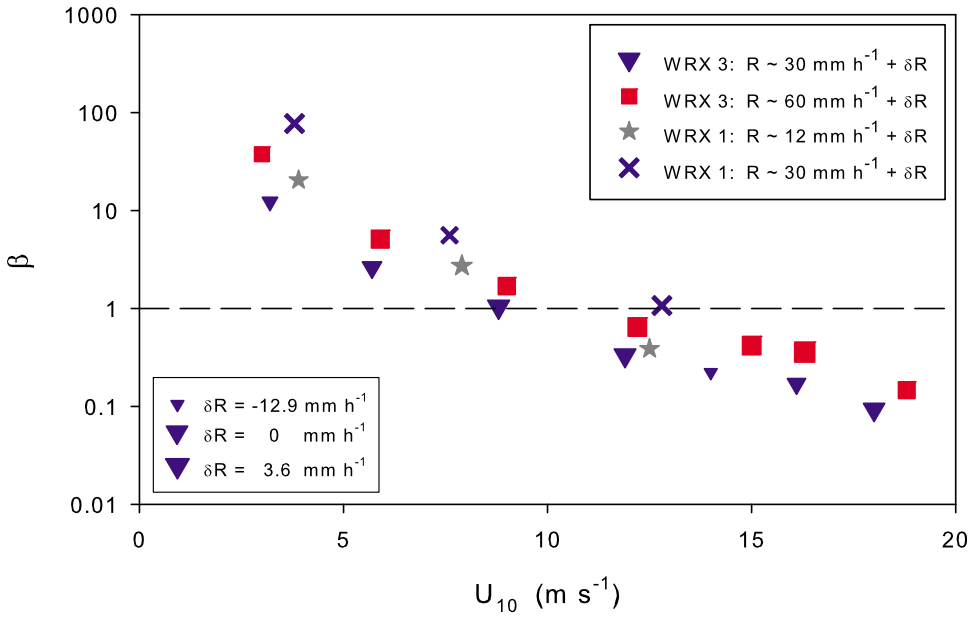

Figure 11. The ratio, β, of the measured rain-imparted vertical kinetic energy flux, KEF_r, to the wind-imparted values, KEF_w, are shown for all rain experiments in the present study. The β values for WRX 1 [*Ho et al.*, 2007] have been plotted for comparison. Symbol size indicates each experiment's rain rate variation, δR, from either 12, 30 or 60 mm h^{-1} with smaller and larger symbols reflecting below and above average rain rates, respectively. Rain effects are observed in both the gas exchange and dynamics measurements when $\beta > 1$ in the present study.

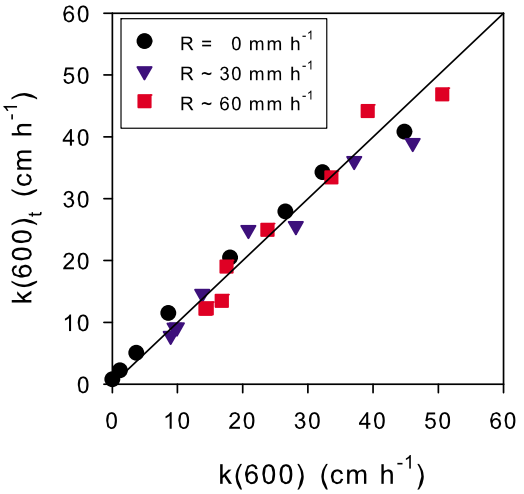

Figure 12. The developed nonlinear model, equation (12), for the combined effect of rain and wind on gas exchange which predicts gas transfer velocities, $k(600)_t$, exhibits a strong correlation with the laboratory data, $k(600)$.

data point, β is always greater than one (Figure 11) indicating that rain might be the predominate gas transfer mechanism. It is interesting to note that the only point from the WRX 1 data set for which $\beta < 1$ corresponds in fact to an outlier in the analysis of *Ho et al.* [2007]; i.e. this data point does not conform to the linearly additive model for which wind and rain influences simply add. We believe that if higher wind speeds had been used during *Ho et al.* [2007], there would have been several cases where $\beta < 1$ and $k(600)$ would not have been linearly additive for rain and wind. In other words, the consistent cutoff wind speed value of 11 m s^{-1} found in this study, after which the rain does not appear to affect the dynamics (Figures 4, 5, and 7), or $k(600)$ (Figure 8), was brought to light by a more extensive set of wind and rain conditions. A far better way to look at the data is to examine it in the context of the kinetic energy flux from the wind, the rain, and their ratio.

[38] We therefore propose a nonlinear model for the total gas transfer velocity, $k(600)_t$, by adding the wind-induced gas transfer velocity, $k(600)_w$ to the rain-generated gas transfer velocity, $k(600)_r$, weighted with a function of β

$$k(600)_t = k(600)_w + \left(1 - e^{-a\beta}\right) k(600)_r, \qquad (12)$$

where $k(600)_w$ and $k(600)_r$ are the wind-induced only, and rain-induced only, gas transfer velocities respectively, and a is a nondimensional e-folding parameter. For the laboratory, using the no rain $k(600)$ data, it was found that $k(600)_w = 0.1414U_{10}^2$, where $r^2 = 0.9759$. The parameter a was determined to be 0.3677 using an iterative least-squares method. The complete nonlinear model above predicts very well ($r^2 = 0.9593$) the observed $k(600)$ values over the whole range of combined wind and rain conditions (Figure 12).

4.3. Extrapolating to Field Conditions

[39] *Ho et al.* [2004] found that the gas transfer velocities generated by rain impacting saltwater were similar to those predicted using the *Ho et al.* [1997] kinetic energy flux relationship developed for freshwater, with only the overall flux reduced due to the presence of stratification effects with

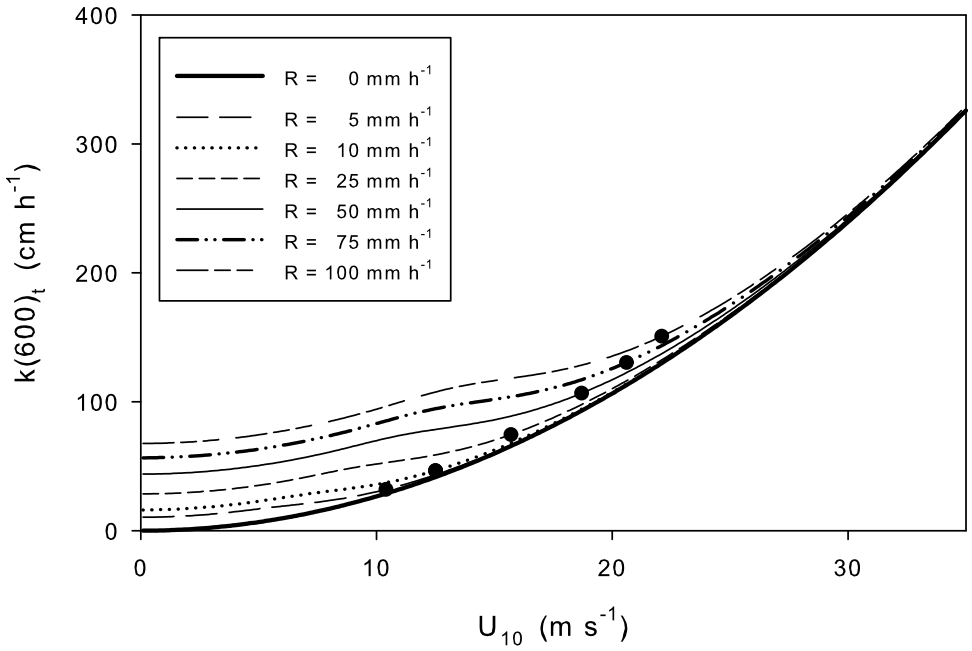

Figure 13. Field estimates of the gas transfer velocity using the new wind-rain joint parameterization (equation (12)). In order to better simulate field conditions, the parameterization of *Ho et al.* [2006] is used here to calculate the wind contribution and the realistic Laws-Parsons drop size distribution is used in the rain contribution calculations. Black circles indicate the wind speed at which the cutoff parameter $\beta = 1$ and rain has a significantly reduced effect on the total air-sea gas exchange.

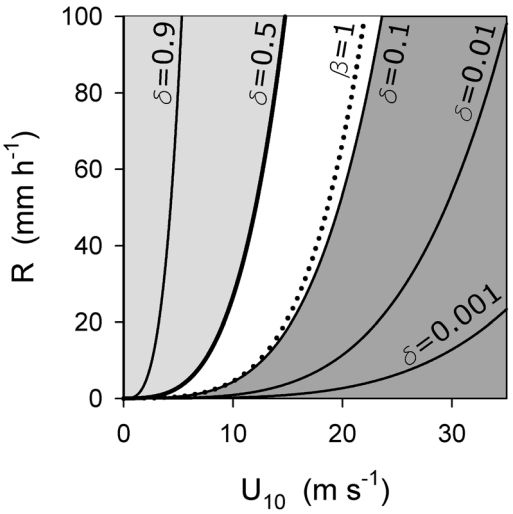

Figure 14. This $R - U_{10}$ phase diagram displays contours of the ratio of the rain contribution to the gas transfer velocity to the total value, δ. Light gray shading indicates δ values in which rain will yield a significant contribution to the total air-sea gas exchange. Dark gray shading indicates δ values in which rain will have no effect on air-sea gas exchange. The white region indicates the conditions where the rain effects will diminish and wind effects will start to dominate. The $\beta = 1$ contour is shown with a dotted line and indicates that the determined cutoff condition for rain effects is successfully reflected in the modeled gas transfer velocity values.

saltwater. Here we have updated the *Ho et al.* [1997] kinetic energy flux-gas transfer velocity relationship to include the results of additional freshwater experiments (equation (10)). We have also shown that the combined effect of rain and wind on the total gas transfer velocity can be modeled using a nonlinear model given in equation (12). Using the nonlinear model presented here, with the knowledge that freshwater and saltwater have similar rain-induced gas transfer velocities, we believe it is then possible to estimate the expected rain-wind combined gas transfer velocities in the field. To determine β for field conditions, the rain-imparted vertical kinetic energy flux, KEF_r, can be calculated for different rain rates with realistic raindrop size distributions, such as the Laws-Parsons distribution, for which the integral calculation (see Appendix A for details) can be further simplified to

$$KEF_r = 0.0112R, \tag{13}$$

where R has the units of mm h^{-1}; this linear regression has an $r^2 = 0.9999$ for the Laws-Parson drop size distribution. The wind-imparted kinetic energy flux can be estimated using the *Zeng et al.* [1998] parameterization for the drag coefficient, C_D, and the relationship

$$u_*^2 = C_D U_{10}^2. \tag{14}$$

Then, after replacing our laboratory parameterization for $k(600)_w$ with the wind speed-gas exchange parameterization of *Ho et al.* [2006], $k(600)_t$ can be calculated for a variety of R and U_{10} field conditions (Figure 13). It should be noted laboratory KEF_r correspond to field KEF_r with rain rates between 3–8.3 mm h^{-1} and the laboratory drop radius is within the peak of the volume flux of rain calculated using the Laws-Parsons drop size distribution. This nonlinear model, when applied to realistic field conditions, predicts that rain will significantly enhance the gas transfer velocity at low wind speeds, when $\beta > 1$. At high wind speeds, where $\beta < 1$ for common rain rates, the rain will have a negligible effect on the total gas flux. This joint wind-rain parameterization exhibits a smooth transition between the rain dominated regime and the wind dominated regime and yields total gas transfer velocities similar to those observed in the laboratory (see Figure 8). These results also compare well with those calculated using the Marshall-Palmer drop size distribution which yields similar, but slightly lower, KEF_r values for identical R values.

[40] In order to generate a guideline for when rain will affect gas exchange, we define the ratio of the gas transfer velocity contribution from rain to the total gas transfer velocity, δ:

$$\delta \equiv \frac{\left(1 - e^{-a\beta}\right) k(600)_r}{k(600)_t}. \tag{15}$$

The parameter δ can be calculated for a full range of R and U_{10} conditions (Figure 14). Rain contributes significantly to the gas transfer velocity when $\delta > 0.5$; the contributions from rain and wind to the gas transfer velocity are equal when $\delta = 0.5$. There is no significant effect of rain on the gas transfer velocity when $\delta < 0.1$. The R and U_{10} conditions when $\delta = 0.1$ are also nearly identical to those when $\beta = 1$, the cutoff limit for rain determined in an earlier section. For example, from this estimate, we can surmise that rain will contribute significantly to air-sea gas exchange when $R = 10$ mm h^{-1} and $U_{10} = 5$ m s^{-1} but will have no effect when $R = 10$ mm h^{-1} and $U_{10} = 15$ m s^{-1}. Evidently, these estimates provide a preliminary assessment for when rain effects matter in the open ocean and still need to be validated with in situ field measurements. Still, considering that much of the ocean surface is in the low wind speed regime, with globally averaged speeds of 6–8 m s^{-1} and with potentially high correlation between high precipitation and low wind speed regions such as the tropics, it is clear that rainfall can impact the global air-sea gas exchange rates. For example, in the tropics, where rain rates are high, O(10) mm h^{-1}, and wind speeds are low, O(5) m s^{-1}, a 2-h period of rain can increase the 24 h air-sea gas exchange rate by O(10%) compared to dry conditions.

5. Conclusions

[41] We performed measurements of the combined rain and wind effect on the air-water gas transfer velocity. The unique experimental setup used here, where rain impacted a large percentage of surface area (≈50%) over the wind wave flume, provided improved experimental conditions over previous laboratory studies. It was found that the rain can have a substantial effect on the total air-water gas flux, especially at low-to-moderate wind speeds. Our results show that rain and wind combine nonlinearly to enhance gas

exchange in freshwater at low to moderate wind speeds. When the ratio of the vertical kinetic energy flux of rain to the kinetic energy flux of wind is approximately equal to 1, we find the rain effect on the total gas flux quickly become negligible. These gas flux results are supported by the measurement of the influence of the rain on the waves, currents and turbulence. Based on these results, we developed a gas transfer model that takes into account both wind and rain effects (nonlinearly) and which appears to model the data very well. When extrapolated to the field, this model can help indicate for which rain and wind speed conditions the rainfall is expected to significantly influence air-sea gas fluxes.

Appendix A

[42] The number distribution of raindroplets, $n(r)$, for a given droplet radius r (and per dr increment), is typically a function of the rain rate R, which is the volume rate of water accumulation per unit surface area [*Caldwell and Elliott*, 1971]. The rain rate is sometimes given in mm h^{-1} for convenience. Here, we choose the Laws-Parsons formulation, $n(r) = n_o R^{-0.384} r^{2.93} e^{-649.142 R^{-0.186} r}$, where n_o is a normalizing factor. Rain droplets are assumed to have a two-dimensional fall velocity, $\overrightarrow{U_r}$, where the vertical component w is the terminal velocity and the horizontal component u is typically, at impact, a fraction of the 10 m wind speed. The rain rate is dependant on terminal velocity and here we use the formulation for w given by *Lhermitte* [1988]:

$$w(r) = 9.25\left(1 - e^{-10^3\left(272r^2 + 0.976r\right)}\right), \tag{A1}$$

where the units of r and w are m and m s^{-1}, respectively.

[43] The raindrop size distribution (along with the raindrop velocities) is quite useful and several parameters can be derived from it. For example, by definition, the total number of droplets per unit volume of air, N, is

$$N = \int_0^\infty n(r)dr. \tag{A2}$$

Consequently, the number of impacts (on a horizontal surface) per unit surface area, per unit time, is simply the droplet number flux, N_o:

$$N_o = \int_0^\infty n(r)w(r)dr. \tag{A3}$$

In addition, the flux, through a horizontal surface, of the rain volume (i.e. the rain rate, R), and of the momentum, MF_{rain}, and that of the kinetic energy from the rain, KEF_{rain}, are, respectively,

$$R = \int_0^\infty \frac{4}{3}\pi r^3 n(r)w(r)dr, \tag{A4}$$

$$MF_{rain} = \int_0^\infty \rho_d \frac{4}{3}\pi r^3 \left|\overrightarrow{U_r}(r)\right| n(r)w(r)dr, \tag{A5}$$

$$KEF_{rain} = \int_0^\infty \frac{1}{2}\rho_d \frac{4}{3}\pi r^3 \left|\overrightarrow{U_r}(r)\right|^2 n(r)w(r)dr, \tag{A6}$$

where ρ_d is the density of raindrops (freshwater).

[44] An estimate of the kinetic energy dissipation due only to rainfall can be completed quickly and yields surprising results. If we assume a droplet's horizontal velocity imparts current to the water similarly to the wind [*Caldwell and Elliott*, 1971], then the vertical component will contribute to the generation of turbulence (a conservative estimate of rain-generated turbulence). When a droplet impacts the water, its vertical kinetic energy will be lost to (1) the generation of a cavity that sometimes traps a bubble when it collapses, (2) the generation of surface gravity-capillary waves, and (3) the generation of turbulence. Note here that the sound produced by rain is essentially generated by the free oscillations of the bubble that is created by the collapse of the cavity. The energy lost to sound waves is therefore accounted for in the energy lost to the creation of the cavity. Also, some kinetic energy is temporarily converted to potential energy when droplets bounce; however, this energy will eventually be once again transferred to the ocean surface as the droplets fall back.

[45] The total amount of mechanical energy available upon impact, the kinetic energy flux of rain, is described by equation (A6); restricting this analysis to the vertical component replaces $\left|\overrightarrow{U_r}(r)\right|$ with $w(r)$. At impact, it has been estimated that approximately 30% of KEF_{rain} is lost to the generation of the cavity [*Liow*, 2001]; therefore, the remaining available energy is

$$KEF_{avail} = 0.7 \times \int_0^\infty \frac{1}{2}\rho_d \frac{4}{3}\pi r^3 w(r)^2 n(r)w(r)dr. \tag{A7}$$

Next, we assume that a droplet of radius r creates a ring wave of height $a = r$ and wavelength $\lambda = 2r$ [*Engel*, 1966; *Schlüssel et al.*, 1997]. Assuming the radius of the ring wave is also the radius of the cavity created, R_c, and is given by [*Prosperetti and Oguz*, 1993]

$$R_c = r\left(2\left(\frac{2}{3}Fr + 4\frac{Fr}{We} + \frac{Fr^2}{We^2}\right)^{\frac{1}{2}} - 2\frac{Fr}{We}\right)^{\frac{1}{2}}, \tag{A8}$$

the total kinetic energy flux lost to the ring wave will be

$$KEF_{wave} = \int_0^\infty \frac{1}{2}\left(\rho_w g + Tk^2\right)a^2 \times 2\pi R_c \lambda n(r)w(r)dr, \tag{A9}$$

where ρ_w is the receiving water's density, T is the surface tension, k is the wavenumber, g is the acceleration due to gravity, $Fr = w^2(2rg)^{-1}$ is the Froude number and $We = \rho_d w^2(2r)T^{-1}$ is the Weber number. The remaining energy available for the generation of turbulence by a droplet, therefore, is

$$KEF_{turb} = \int_0^\infty \left(0.7 \times \frac{1}{2}\rho_d \frac{4}{3}\pi r^3 w(r)^2 - \left(\rho_w g + Tk^2\right)a^2 \pi R_c \lambda\right) \cdot n(r)w(r)dr. \tag{A10}$$

Using this estimate and assuming that the total kinetic energy provided by the rain is confined to a layer of depth D, the turbulent kinetic energy dissipation, ε, in that layer (and under a rain rate of R) can be estimated:

$$\varepsilon = \int_0^\infty \frac{1}{\rho_w D}\left(0.7 \times \frac{1}{2}\rho_d \frac{4}{3}\pi r^3 w(r)^2 - \left(\rho_w g + Tk^2\right)a^2 \pi R_c \lambda\right) \cdot n(r)w(r)dr. \quad \text{(A11)}$$

When equation (A11) is evaluated for a range of rain rates and a mixed layer depth D of O(20) cm [*Green and Houk*, 1979], we find that the depth-averaged kinetic energy dissipation is $\varepsilon \approx$ O(10^{-5}–10^{-3}) m^2 s^{-3}. For example, we have $\varepsilon \approx 3.6 \times 10^{-5}$, 3.7×10^{-4} and 1.9×10^{-3} m^2 s^{-3} for rain rates of 1, 10, and 50 mm h^{-1}, respectively. These values are rather large, especially when compared to other dissipation measurements in the open ocean. Dissipation values range from $\varepsilon \approx 10^{-8}$ m^2 s^{-3} in the open ocean to $\varepsilon \approx 10^{-3}$ m^2 s^{-3} in the surf zone [*George et al.*, 1994; *Veron and Melville*, 1999], with typical values in the upper 5 m of the ocean in the range of $\varepsilon \approx 10^{-5}$–$10^{-4}$ m^2 s^{-3} depending on wind speed [*Anis and Moum*, 1995; *Drennan et al.*, 1996; *Terray et al.*, 1996; *Veron and Melville*, 1999]. Also, while the energy required to create a cavity and bubble was taken out of this estimate, with regard to the gas transfer, the creation of a bubble, besides the obvious bubble-fluid transfers, will only add to the turbulence in enhancing air-sea gas transfer rates.

[46] **Acknowledgments.** We thank D. Di Leonardo, E. McMahon, D. Turk, and J. De Lanoy for assistance during the experiment and S. Eggleston for help with data analysis. Funding was provided by the National Science Foundation through OCE 06-48171 (F.V.) and OCE 09-30057 (D.T.H.). This is LDEO contribution 7521.

References

Anis, A., and J. N. Moum (1995), Surface wave-turbulence interactions: Scaling ϵ(z) near the sea surface, *J. Phys. Oceanogr.*, *25*, 2025–2045.

Bliven, L. F., P. W. Sobieski, and C. Craeye (1997), Rain generated ring-waves: Measurements and modelling for remote sensing, *Int. J. Remote Sens.*, *18*, 221–228.

Braun, N., M. Gade, and P. A. Lange (2002), The effect of artificial rain on wave spectra and multi-polarisation X band radar backscatter, *Int. J. Remote Sens.*, *23*, 4305–4323.

Brumley, B. H., and G. H. Jirka (1987), Near-surface turbulence in a grid-stirred tank, *J. Fluid Mech.*, *183*, 235–263.

Caldwell, D. R., and W. P. Elliott (1971), Surface stresses produced by rainfall, *J. Phys. Oceanogr.*, *1*, 145–148.

Drennan, W. M., M. A. Donelan, E. A. Terray, and K. B. Katsaros (1996), Oceanic turbulence dissipation measurements in SWADE, *J. Phys. Oceanogr.*, *26*, 808–815.

Engel, O. G. (1966), Crater depth in fluid impacts, *J. Appl. Phys.*, *37*, 1798–1808.

Gemmrich, J. R., and D. M. Farmer (2004), Near-surface turbulence in the prescence of breaking waves, *J. Phys. Oceanogr.*, *34*, 1067–1086.

George, R., R. E. Flick, and R. T. Guza (1994), Observations of turbulence in the surf zone, *J. Geophys. Res.*, *99*, 801–810.

Green, T., and D. F. Houk (1979), The mixing of rain with near-surface water, *J. Fluid Mech.*, *90*, 569–588.

Ho, D. T., L. F. Bliven, R. Wanninkhof, and P. Schlosser (1997), The effect of rain on air-water gas exchange, *Tellus*, *49*, 149–158.

Ho, D. T., W. E. Asher, L. F. Bliven, P. Schlosser, and E. L. Gordan (2000), On mechanisms of rain-induced air-water gas exchange, *J. Geophys. Res.*, *105*, 24,045–24,057.

Ho, D. T., C. J. Zappa, W. R. McGillis, L. F. Bliven, B. Ward, J. W. H. Dacey, P. Schlosser, and M. B. Hendricks (2004), Influence of rain on air-sea gas exchange: Lessons from a model ocean, *J. Geophys. Res.*, *109*, C08S18, doi:10.1029/2003JC001806.

Ho, D. T., C. S. Law, M. J. Smith, P. Schlosser, M. Harvey, and P. Hill (2006), Measurements of air-sea gas exchange at high wind speeds in the Southern Ocean: Implications for global parameterizations, *Geophys. Res. Lett.*, *33*, L16611, doi:10.1029/2006GL026817.

Ho, D. T., F. Veron, E. Harrison, L. F. Bliven, N. Scott, and W. R. McGillis (2007), The combined effect of rain and wind on air-water gas exchange: A feasibility study, *J. Mar. Syst.*, *66*, 150–160.

Jähne, B., W. Huber, A. Dutzi, T. Wais, and J. Ilmberger (1984), Wind/wave-tunnel experiment on the schmidt number and wave field dependence of air/water gas exchange, in *Gas Transfer at Water Surfaces*, edited by W. Brutsaert and G. H. Jirka, pp. 303–309, D. Reidel, Norwell, Mass.

Jähne, B., K. O. Münnich, R. Bosinger, A. Dutzi, W. Huber, and P. Libner (1987), On parameters influencing air-water gas exchange, *J. Geophys. Res.*, *92*, 10,767–10,776.

Ledwell, J. J. (1984), The variation of the gas transfer coefficient with molecular diffusity, in *Gas Transfers at Water Surfaces*, edited by W. Brutsaert and G. H. Jirka, pp. 293–302, D. Reidel, Hingham, Mass.

Lhermitte, R. M. (1988), Observation of rain at vertical incidence with a 94 GHz Doppler radar: An insight on Mie scattering, *Geophys. Res. Let.*, *15*, 1125–1128.

Liow, J. L. (2001), Splash formation by spherical drops, *J. Fluid Mech.*, *427*, 73–105.

Lumley, J. L., and E. A. Terray (1983), Kinematics of turbulence convected by a random wave field, *J. Phys. Oceanogr.*, *13*, 2000–2007.

Nightingale, P. D., G. Malin, C. S. Law, A. J. Watson, P. S. Liss, M. I. Liddicoat, J. Boutin, and R. C. Upstill-Goddard (2000), In situ evaluation of air-sea gas exchange parameterizations using novel conservative and volatile tracers, *Global Biogeochem. Cycles*, *14*, 373–387.

Poon, Y. K., S. Tang, and J. Wu (1992), Interactions between rain and wind waves, *J. Phys. Oceanogr.*, *22*, 976–987.

Prosperetti, A., and H. N. Oguz (1993), The impact of drops on liquid surfaces and the underwater noise of rain, *Annu. Rev. Fluid Mech.*, *25*, 577–602.

Reynolds, O. (1875), On the action of rain to calm the sea, *Pop. Sci. Mon.*, *6*, 732–734.

Schlüssel, P., A. V. Soloviev, and W. J. Emery (1997), Cool and freshwater skin of the ocean during rainfall, *Boundary Layer Meteorol.*, *82*, 439–474.

Takagaki, N., and S. Komori (2007), Effects of rainfall on mass transfer across the air-water interface, *J. Geophys. Res.*, *112*, C06006, doi:10.1029/2006JC003752.

Terray, E. A., M. A. Donelan, Y. C. Agrawal, W. M. Drennan, K. K. Kahma, A. J. Williams, P. A. Hwang, and S. A. Kitaigorodskii (1996), Estimates of kinetic energy dissipation under breaking waves, *J. Phys. Oceanogr.*, *26*, 792–807.

Tsimplis, M. N. (1992), The effect of rain in calming the sea, *J. Phys. Oceanogr.*, *22*, 404–412.

Tsimplis, M., and S. A. Thorpe (1989), Wave damping by rain, *Nature*, *342*, 893–895.

Turk, D., C. J. Zappa, C. S. Meinen, J. R. Christian, D. T. Ho, A. G. Dickson, and W. R. McGillis (2010), Rain impacts on CO_2 exchange in the western equatorial Pacific Ocean, *Geophys. Res. Lett.*, *37*, L23610, doi:10.1029/2010GL045520.

Veron, F., and W. K. Melville (1999), Pulse-to-pulse coherent Doppler measurements of waves and turbulence, *J. Atmos. Oceanic Technol.*, *16*, 1580–1597.

Wanninkhof, R. (1992), Relationship between wind speed and gas exchange over the ocean, *J. Geophys. Res.*, *97*, 7373–7382.

Wanninkhof, R., J. R. Ledwell, W. S. Broecker, and M. Hamilton (1987), Gas exchange on Mono lake and Crowley lake, California, *J. Geophys. Res.*, *92*, 14,567–14,580.

Wanninkhof, R., W. E. Asher, D. T. Ho, C. Sweeney, and W. R. McGillis (2009), Advances in quantifying air-sea gas exchange and environmental forcing, *Annu. Rev. Mar. Sci.*, *1*, 213–244.

Yang, Z., S. Tang, and J. Wu (1997), An experimental study of rain effects on fine structures of wind waves, *J. Phys. Oceanogr.*, *27*, 419–430.

Zappa, C. J., D. T. Ho, W. R. McGillis, M. L. Banner, J. W. H. Dacey, L. F. Bliven, B. Ma, and J. Nystuen (2009), Rain-induced turbulence and air-sea gas transfer, *J. Geophys. Res.*, *114*, C07009, doi:10.1029/2008JC005008.

Zeng, X., M. Zhao, and R. E. Dickinson (1998), Intercomparison of bulk aerodynamic algorithms for the computation of sea surface fluxes using TOGA COARE and TAO data, *J. Clim.*, *11*, 2628–2644.

E. L. Harrison, College of Earth, Ocean and Environment, University of Delaware, 700 Pilottown Rd., Lewes, DE 19958, USA. (elh@udel.edu)

D. T. Ho, School of Ocean and Earth Science and Technology, Department of Oceanography, University of Hawai'i at Manoa, 1000 Pope Rd., MSB 517, Honolulu, HI 96822, USA.

W. R. McGillis, Lamont-Doherty Earth Observatory of Columbia University, 413 Comer, 61 Route 9W, PO Box 1000, Palisades, NY 10964-8000, USA.

P. Orton, Stevens Institute of Technology, 613 Babbio Center, 555 River St., Hoboken, NJ 07030, USA.

M. Reid, Department of Civil and Environmental Engineering, Princeton University, E308 Engineering Quad, Princeton, NJ 08544, USA.

F. Veron, College of Earth, Ocean and Environment, University of Delaware, 112C Robinson Hall, Newark, DE 19716, USA.